Advanced Composite Materials
Publication details, including instructions for authors and subscription information:
http://www.tandfonline.com/loi/tacm20

Detecting an Arrested Crack in a Foam-Core Sandwich Structure Using an Optical Fiber Sensor Embedded in a Crack Arrester

Shu Minakuchi [a], Ippei Yamauchi [b], Nobuo Takeda [c] & Yasuo Hirose [d]

[a] Department of Advanced Energy, Graduate School of Frontier Sciences, The University of Tokyo, 5-1-5 Kashiwanoha, Kashiwa-shi, Chiba, 277-8561, Japan;, Email: minakuchi@smart.k.u-tokyo.ac.jp

[b] Department of Aeronautics and Astronautics, School of Engineering, The University of Tokyo, 7-3-1 Hongo, Bunkyo-ku, Tokyo, 113-8656, Japan

[c] Department of Advanced Energy, Graduate School of Frontier Sciences, The University of Tokyo, 5-1-5 Kashiwanoha, Kashiwa-shi, Chiba, 277-8561, Japan

[d] Commercial Aircraft Project Engineering Division, Aerospace Company, Kawasaki Heavy Industries, Ltd., 1 Kawasaki-cho, Kakamigahara-shi, Gifu, 504-8710, Japan

Version of record first published: 02 Apr 2012.

VSP

Advanced Composite Materials 20 (2011) 419–433

ADVANCED COMPOSITE MATERIALS
brill.nl/acm

Detecting an Arrested Crack in a Foam-Core Sandwich Structure Using an Optical Fiber Sensor Embedded in a Crack Arrester

Shu Minakuchi [a,*], **Ippei Yamauchi** [b], **Nobuo Takeda** [a] **and Yasuo Hirose** [c]

[a] Department of Advanced Energy, Graduate School of Frontier Sciences, The University of Tokyo, 5-1-5 Kashiwanoha, Kashiwa-shi, Chiba, 277-8561, Japan

[b] Department of Aeronautics and Astronautics, School of Engineering, The University of Tokyo, 7-3-1 Hongo, Bunkyo-ku, Tokyo, 113-8656, Japan

[c] Commercial Aircraft Project Engineering Division, Aerospace Company, Kawasaki Heavy Industries, Ltd., 1 Kawasaki-cho, Kakamigahara-shi, Gifu, 504-8710, Japan

Received 30 September 2010; accepted 11 February 2011

Abstract

A crack arrester was recently developed to suppress crack propagation along the interface between the facesheet and the core in a foam-core sandwich structure. The crack arrester is a semi-cylindrical stiff material inserted into the interface. The crack arrester decreases the energy release rate at the crack tip by suppressing local deformation around the crack. If the arrested crack can be instantaneously detected, the damage tolerance of foam-core sandwich structures can be dramatically improved. This study establishes an innovative crack detection technique using two fiber Bragg grating (FBG) sensors embedded at both edges of the arrester. The change in strain distribution in the crack arrester induced by arresting the crack is evaluated using reflection spectra from the FBG sensors. The proposed technique enables an effective application of the crack arrester and significantly improves the reliability of foam-core sandwich structures.

Keywords

Foam-core sandwich, interface crack, crack arrester, structural health monitoring, optical fiber sensors

1. Introduction

Carbon fiber reinforced plastic (CFRP) is used for almost all modern commercial aircraft as a primary structural material. However, the potential capability of CFRP cannot be maximized under the conventional structural design concept, which consists of skins, stringers and frames. One innovative structural concept is a foam-core sandwich panel structure [1–5]. The integral construction consists of two thin

* To whom correspondence should be addressed. E-mail: minakuchi@smart.k.u-tokyo.ac.jp

 DOI:10.1163/092430411X568205

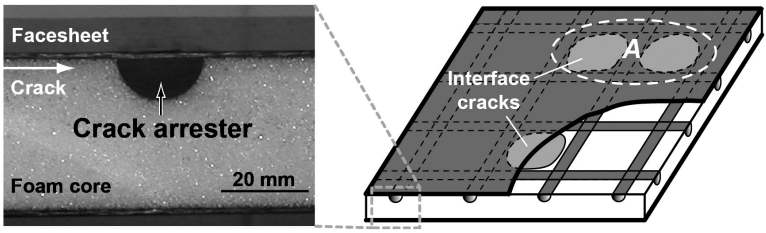

Figure 1. Crack arrester.

Figure 2. Distribution of normal stress in the vertical direction depending on crack tip position.

facesheets and a lightweight foam core, which can considerably reduce the weight and the number of parts compared to conventional structures. However, crack propagation along the interface between the facesheet and the core is a critical issue [6–13]. An interface crack originates from manufacturing defects, impact damage or fatigue shear cracks in the foam core. A crack below the facesheet is difficult to detect using conventional non-destructive inspection techniques. However, the interface crack seriously degrades structural integrity. Thus, Hirose *et al.* developed a crack arrester (Fig. 1) [14], which is a semi-cylindrical stiff material inserted into the interface. When a crack approaches the arrester, the arrester decreases the energy release rate at the crack tip by suppressing local deformation around the crack. Figure 2 illustrates the distribution of the normal stress in the vertical direction, calculated in finite-element analysis. As the crack approaches the crack arrester, the stress at the crack-side edge of the arrester gradually increases; consequently, stress concentration at the crack tip is reduced. In practical applications, the arrester is arranged in a grid pattern, and the interface crack is trapped inside the grid (Fig. 1). Suppression of crack propagation has been evaluated under various loading conditions, confirming that the crack arrester improves damage tolerance of foam-core sandwich structures [14–16].

In designing structures with a crack arrester, the arrester grid interval may be determined from the maximum allowable crack size. An appropriately designed structure operates safely while tolerating a crack trapped inside the grid. For practical use, however, the arrested crack should be instantaneously detected, and appropriate countermeasures must be taken against the damaged area. Arrested but undetected cracks induced from different damage in neighboring grids or, more critically, adjoining grids (*A* in Fig. 1) significantly degrade mechanical properties and increase the stress around these grids. As a result, an area without a crack may fail and/or

undetected cracks may penetrate the arresters, leading to catastrophic failure of the entire structure.

This study establishes an innovative crack detection technique using fiber Bragg grating (FBG) sensors embedded in a co-cured, semi-cylindrical crack arrester to locate grids with an arrested crack immediately after its occurrence, and improves damage tolerance of foam-core sandwich structures. We begin by proposing the crack detection technique, and then conduct numerical analysis to predict the sensor response due to crack propagation and to validate the feasibility of the proposed technique. Finally, the technique is verified by experiments.

2. Crack Detection Technique

Figure 3 schematically illustrates the crack detection technique. As presented in Fig. 2, stress is induced at the crack-side edge of the arrester when a crack approaches. As a result, stress concentration at the tip of the crack is reduced, preventing crack propagation. In this study, two optical fibers with FBG sensors are aligned parallel to the arrester grid line and embedded at both side edges of the crack arrester, where the strain increases as a crack approaches the arrester. The change in strain distribution induced by suppressing crack propagation is evaluated using the FBG sensors. The FBG sensor has a periodic variation in the refractive index along the length of a single mode optical fiber [17]. When broadband light is launched into the FBG sensor, a narrow spectral component is reflected back, and the reflection spectrum gives the measure of strain and/or temperature. When stress is distributed at the edge of the arrester, a non-axisymmetric strain state arises at the core of the FBG sensor, and the reflection spectrum from the sensor splits into two peaks due to a birefringence effect [18–20]. The difference between the cen-

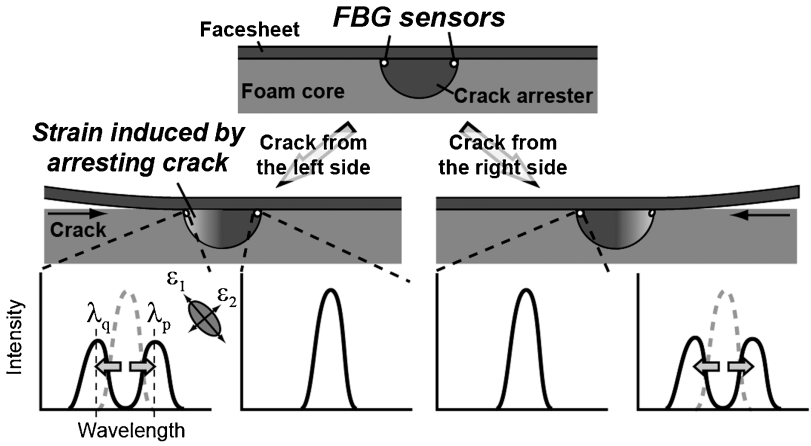

Figure 3. Schematic of crack detection technique.

tral wavelengths $\Delta\lambda$ of the two peaks, λ_p and λ_q ($\lambda_p > \lambda_q$), is calculated using the following equation:

$$\Delta\lambda = \lambda_p - \lambda_q = \frac{n_0^2 \lambda_0}{2}(p_{12} - p_{11})(\varepsilon_1 - \varepsilon_2), \tag{1}$$

where λ_0 is the center wavelength of the initial reflection spectrum, n_0 is the initial refractive index of the optical fiber core, p_{11} and p_{12} are the photoelastic constants and ε_1 and ε_2 are the maximum and minimum principal strains at the core in the cross-sectional direction of the FBG sensor (Fig. 3). This equation indicates that the difference between the center wavelengths of the two peaks is proportional to the difference between the maximum and minimum principal strains at the core. Since the change in the principal strain is greater at the crack-side edge than at the opposite edge, the crack propagation direction can be determined by comparing reflection spectra from the two FBG sensors embedded at both side edges of the crack arrester.

In this study, Mode I and Mode II type cracks are evaluated using beam-type specimens. First, finite-element analysis (FEA) was conducted on a double-cantilever beam (DCB) and end-notch flexure (ENF) sandwich specimens to calculate the change in the maximum and minimum principal strains. The reflection spectrum is simulated based on the calculated strain values.

3. Finite-Element Analysis

3.1. Finite-Element Model

Figure 4 presents 2-D finite-element models with interface cracks modeled in ABAQUS 6.6. Plane strain was assumed, and thermal deformation was considered (curing temperature 130°C). Sizes of the elements differed according to their location. Representative element size around the crack tip and the arrester edges was

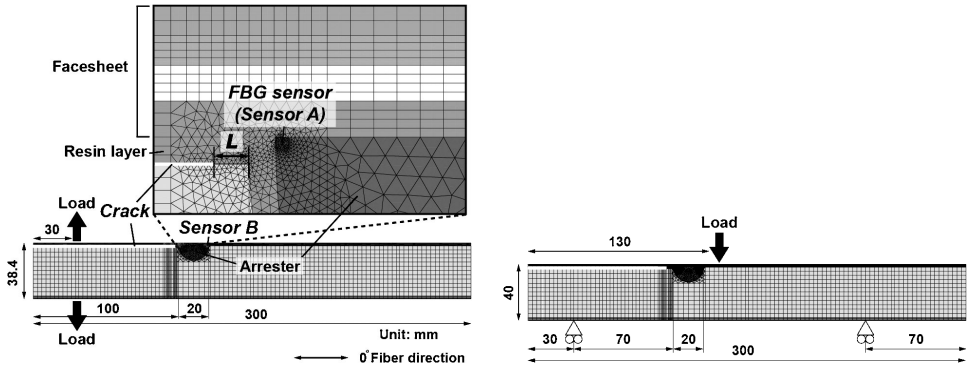

Figure 4. Finite-element models. (a) DCB specimen, (b) ENF specimen.

10 μm, and the other parts consisted of 5 mm-long elements. Due to restriction of the experiment facilities, the DCB and ENF specimens had different material configurations.

The DCB specimen consisted of CFRP facesheets (UT500/#135, Toho Tenax Co. Ltd., [(+45, −45)/(0, 90)/(0, 90)/(+45, −45)], thickness 1.68 mm), a foam core (PMI Rohacell WF-110, Evonik Rohm GmbH, thickness 35 mm), and a semi-cylindrical crack arrester (UT500/#135, Toho Tenax Co. Ltd., unidirectional prepreg, radius 10 mm). The fiber direction of the arrester was perpendicular to the direction of the crack propagation (i.e., parallel to the arrester grid line). In Ref. [14], a microscopic observation of foam-core sandwich specimens revealed that the resin from the facesheet impregnated into cells of the foam core adjacent to the facesheet, and a 0.34 mm-thick resin layer was formed. An interfacial crack (thickness 10 μm) propagated between this resin-impregnated layer and the original foam core. In this study, finite-element models were developed based on this observation. The distance between the crack tip and the crack arrester, L, was set as 10, 5 or 0 mm to investigate the influence of crack propagation on the principal strains.

The ENF specimen consisted of CFRP facesheets (T700S/2500, Toray Industries, Inc., $[0/90]_{5S}$, thickness 2.5 mm), a foam core (PMI Rohacell WF-110, Evonik Rohm GmbH, thickness 35 mm), and a semi-cylindrical crack arrester (HC 9872 SynCore, Hysol Aerospace Products., radius 10 mm). The value of L was set as 20, 10 or 0 mm. The mechanical properties used in the analysis are summarized in Table 1. Different materials were utilized for the crack arrester in the two specimens. As concluded in Ref. [14], both UD CFRP and SynCore are candidate materials for the crack arrester, since they have a higher modulus than that of the foam core and are expected to sufficiently suppress crack propagation. These two materials have similar mechanical properties in the cross-sectional direction of the FBG sensor; thus, material selection does not significantly affect the obtained results. The load applied to each specimen was determined based on fracture loads obtained in preliminary tests: 2.0 N/mm was applied to the DCB specimens, and 60.0 N/mm was applied to the ENF specimens. Two polyimide-coated FBG sensors were embedded at both side edges of the crack arrester along the specimen width direction, to be parallel to the arrester grid line. The cladding diameter of the FBG sensor was 125 μm, and its outside diameter was 150 μm. The cladding and the core of the FBG sensor were modeled as an isotropic material with the property of fused silica glass, and the strain at the center of the optical fiber was defined as the strain at the core. The strain state obtained from the center of the optical fiber was used to calculate the maximum and minimum principal strains at the core (i.e., ε_1 and ε_2 in equation (1)), and these principal strain values were then utilized to simulate the spectral response of the FBG sensor, as will be presented in the next section. 'Sensor A' is the one embedded at the crack side, and 'Sensor B' is the one at the opposite side.

Table 1.
Material properties used in analysis

		UT500/#135 (0, 90)	UT500/#135 Unidirectional	T700S/2500 Unidirectional	HC 9872 SynCore	Rohacell WF-110	Resin layer	Cladding and core	Polyimide coating
Elastic moduli (GPa)	E_{11}	54.9	127	130.1	2.41	0.167	4.1	73.1	1.5
	E_{22}	8.61	8.61	8.03					
	E_{33}	54.9	8.61	8.03					
	G_{12}	3.77	4.23	4.8	1.03	0.071	1.54	31.5	0.60
	G_{23}	3.77	2.78	2.7					
	G_{12}	3.53	4.23	4.8					
Poisson's ratio	ν_{12}	0.33	0.33	0.31	0.167	0.18	0.33	0.16	0.25
	ν_{23}	0.052	0.55	0.49					
	ν_{13}	0.051	0.33	0.31					
Thermal expansion coefficient ($\times 10^{-6}/°C$)	α_{11}	5.0	−1.0	0.30	20	30.7	36	0.5	15
	α_{22}	36.0	36.0	36.5					
	α_{33}	5.0	36.0	36.5					

3.2. Results

Figure 5 plots the obtained principal strains ε_1 and ε_2 in the FBG sensors. In the DCB specimen (Fig. 5(a)), as a crack approached the arrester, the difference between the maximum and minimum principal strains increased in Sensor A at the crack side. Figure 6 schematically illustrates the deformation obtained from the FEA. The facesheet tensile deformation due to local bending induced shear deformation of the crack-side edge of the arrester and thus of the embedded FBG sensor, increasing the maximum principal strain (Fig. 5(a)). In the sensor at the opposite side of the crack, however, both the maximum and minimum principal strains were almost constant. It is important to note that the strain induced in Sensor B at the opposite side of the crack was not mechanical strain but thermal residual strain. This result was confirmed by FEA without applying the mechanical load. The strain state of Sensor B did not change with changes in the applied load. These results suggest

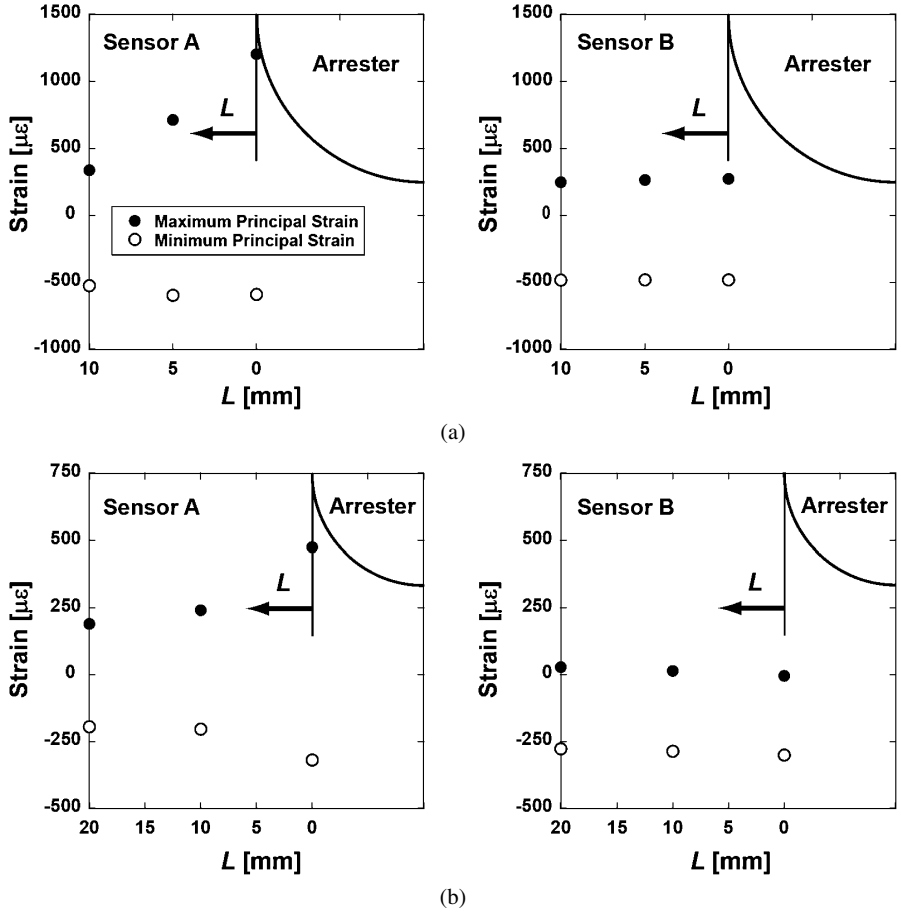

Figure 5. Principal strains in the optical fiber core depending on L. (a) DCB specimen, (b) ENF specimen.

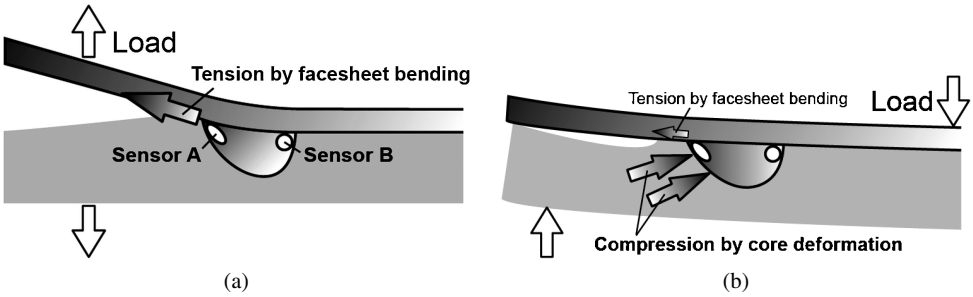

Figure 6. Schematics of sensor deformation demonstrated in FEA. (a) DCB specimen, (b) ENF specimen.

that only the arrester edge at the crack side contributes to suppressing crack propagation. In the ENF specimen, however, the crack arrester was compressed by the core, again inducing shear deformation of the crack-side edge of the arrester and thus of the embedded optical fiber (Fig. 6(b)). As a result, the difference between the maximum and minimum principal strains increased in Sensor A at the crack side (Fig. 5(b)).

Next, the reflection spectra were simulated. First, the difference between the two peak wavelengths $\Delta\lambda$ was calculated from equation (1) with $n_0 = 1.449$, $\lambda_0 = 1550$ nm, $p_{12} = 0.252$ and $p_{11} = 0.113$. The reflection spectrum disturbed by the birefringence effect was then obtained by superpositioning the two power spectra $\Delta\lambda$ away from each other [19, 20]. The initial power spectra of the FBG sensors used in the verification tests (next section) were utilized for the calculation. Figure 7 presents the simulated spectra. The intensity of each spectrum is normalized by the intensity of the highest component in the initial spectrum before embedding. In addition, to clearly compare the spectrum shapes, the wavelength is expressed by the detuning from the peak wavelength of each spectrum. In both the DCB and the ENF specimens, the reflection spectrum from the FBG sensor at the crack side (Sensor A) is clearly split into two peaks as the crack approaches the arrester; thus, the difference between the principal strains increases (Fig. 5). However, the reflection spectra from the FBG sensor opposite the crack (Sensor B) hardly change. Hence, it is expected that crack propagation can be detected by comparing the spectra obtained from the FBG sensors embedded at both edges of the arrester. The next session discusses verification tests using the DCB and ENF specimens.

4. Verification Test

4.1. Materials and Methods

The experiment setups are depicted in Fig. 8. The configurations of the specimens were the same as the ones used in the FEA. The DCB (ENF) specimen was 10 cm (5 cm) wide. The facesheets and the arrester were co-cured with the foam core in an autoclave. Two FBG sensors (grating length 15 mm) were embedded in the arrester

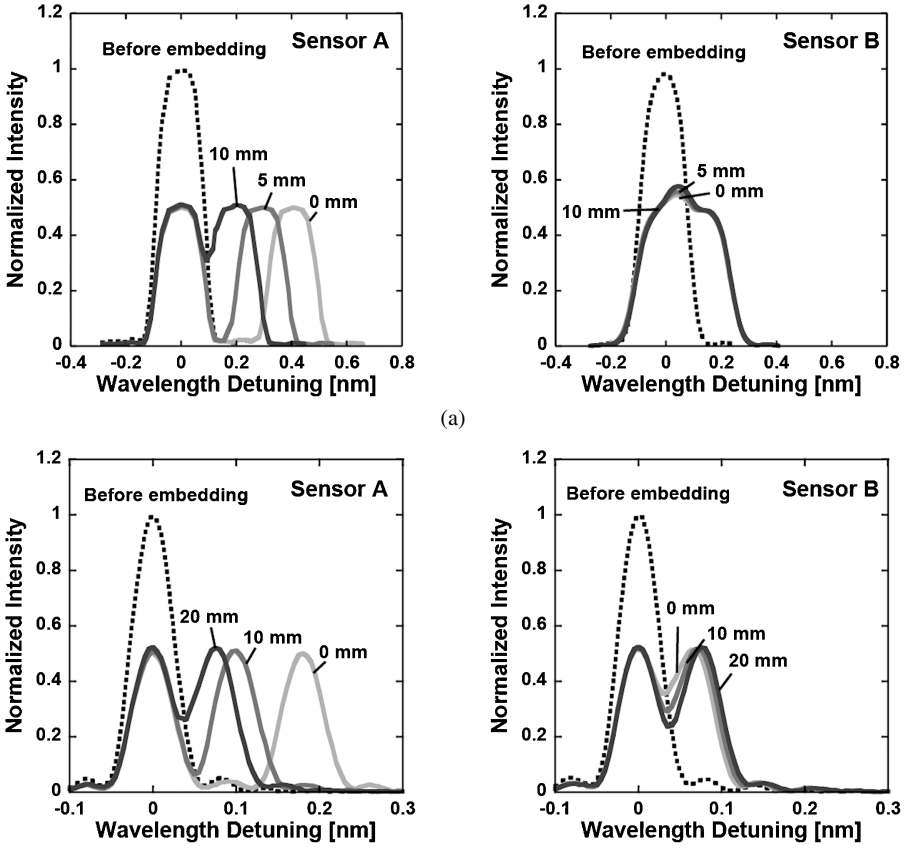

Figure 7. Simulated reflection spectra. (a) DCB specimen, (b) ENF specimen.

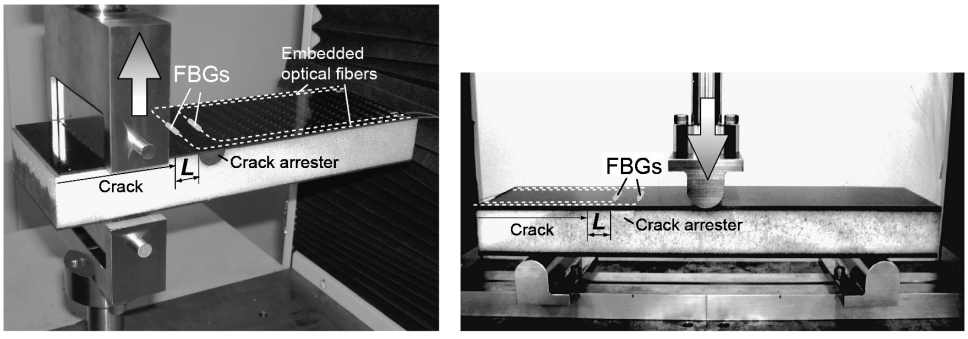

(a) (b)

Figure 8. Experiment setups. (a) DCB test, (b) ENF test.

in contact with the facesheet. The initial crack was introduced by inserting a piece of 0.01 mm-thick polyimide film. The length of the initial crack was 80 mm, and the

distance between the crack tip and the crack arrester, L, was 20 mm. The specimens were loaded at a constant crosshead speed of 2.0 mm/min using a material testing system (AG-50kNI, Shimazu Co.). Once the crack propagated, the test machine was stopped, and the reflection spectra from the two FBG sensors were recorded. The test was then resumed, and this procedure was repeated until the crack reached the arrester edge. The optical fiber was illuminated by an amplified spontaneous emission (ASE) light source (AQ4310(155), Ando Electric Co. Ltd.), and the reflection spectra from the FBGs were measured by an optical spectrum analyzer (AQ6317, Ando Electric Co. Ltd).

4.2. Results and Discussion

Figure 9 presents reflection spectra obtained in the DCB test. The intensity of the spectra before embedding is normalized by the intensity of the highest component. Also, the intensity of the spectrum at each L is normalized by the maximum intensity of the spectrum just after embedding ($L = 20$ mm). For a clear comparison, the wavelength is expressed by detuning from the peak wavelength of each spectrum. Before the test, the spectrum from the FBG sensor at the crack side (Sensor A) had two peaks, due to thermal residual strain. However, several peaks were observed in the spectrum from the sensor opposite the crack (Sensor B), probably due to misalignment of the FBG sensor. Since the optical fiber was severely deflected near the side edge of the beam-type specimen (Fig. 8), the position of the optical fiber partially deviated from the desired position (i.e., the edge of the crack arrester). Consequently, non-uniform strain distribution was induced along the entire length of the FBG sensor, introducing several peaks in the reflection spectrum [21]. It is important to note that misalignment of the sensor is a problem that is unique to the beam-type specimen and thus will not occur in a practical plate-type structure. When the crack approached the arrester, the spectrum from Sensor A clearly split into two peaks ($L = 6.5$ mm). However, the spectrum from Sensor B changed less. These changes in the two spectra are consistent with the result of the FEA, confirming the validity of the proposed technique in Mode I type crack detection. However, when the crack reached the arrester edge ($L = 0$ mm), the spectrum from the crack-side sensor (Sensor A) abruptly recovered its original shape: the two peaks united into one. FEA could not estimate this spectral response; thus, it assessed that internal damage, which the simulation in the previous section did not consider, was induced around the sensor. This recovery of the original spectrum shape was further investigated in the forthcoming part.

The ENF test results are plotted in Fig. 10. Only the spectra obtained from the sensor at the crack-side edge (Sensor A) are plotted, since the opposite side sensor (Sensor B) exhibited almost no changes in spectrum shape, as was also seen in the DCB test. The intensity of the spectra was normalized by the maximum intensity of the spectrum before embedding. As the crack approached the arrester, the difference between the two peak wavelengths gradually increased. The measured spectral response agreed well with the ENF simulation results (Fig. 7(b)), thus confirming

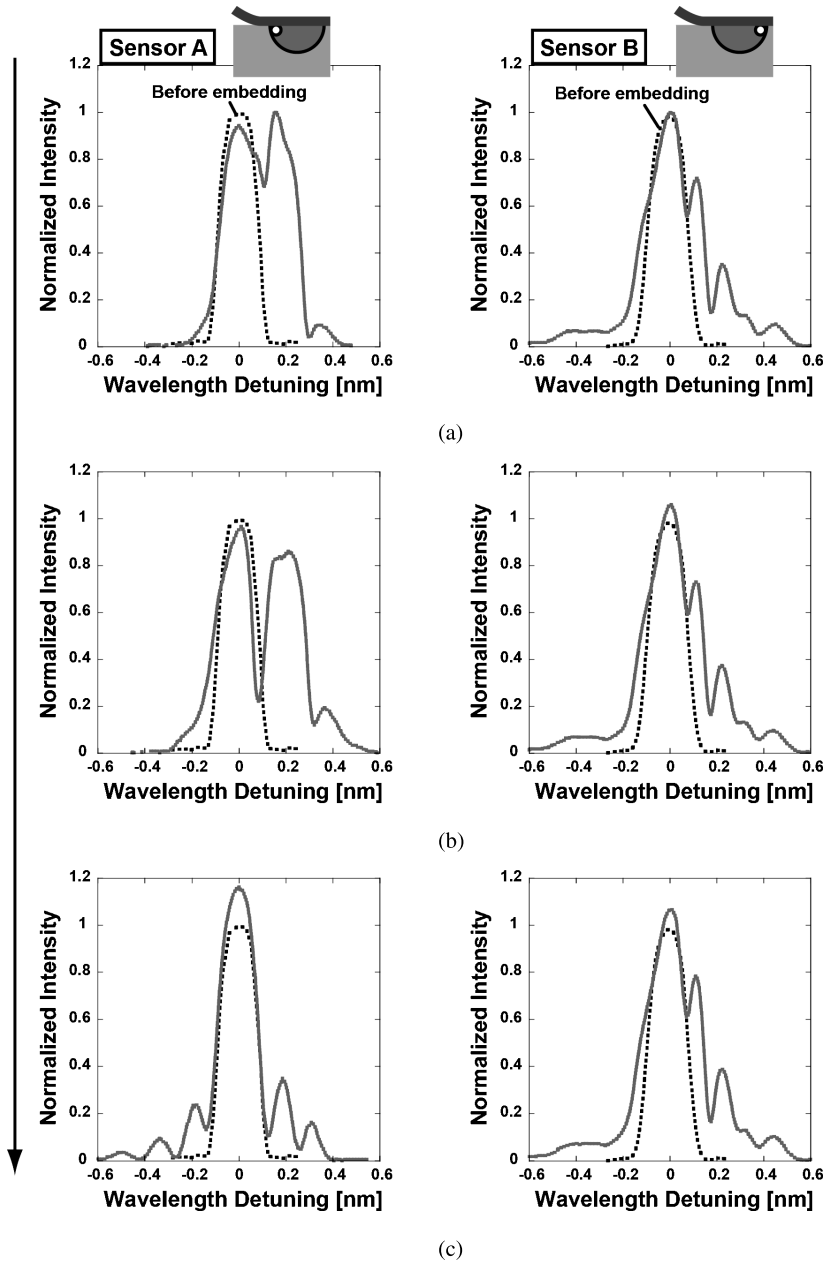

Figure 9. Reflection spectra measured in the DCB test. (a) $L = 20$ mm, (b) $L = 6.5$ mm, (c) $L = 0$ mm.

the validity of the proposed technique in Mode II type crack detection. However, the spectrum again recovered its shape when the crack reached the arrester edge. The observed recovery of the original spectrum shape, as was also observed for the DCB specimen, was further investigated next.

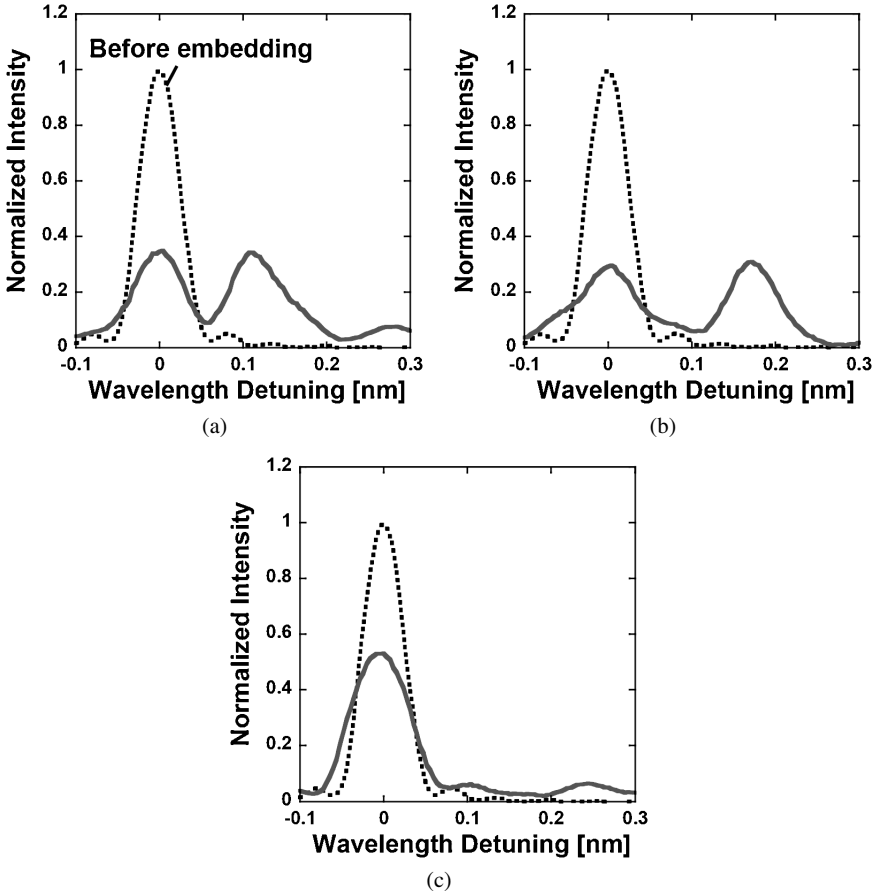

Figure 10. Reflection spectra measured from Sensor A in the ENF test. (a) $L = 20$ mm, (b) $L = 10$ mm, (c) $L = 0$ mm.

After the test, a cross-section of the embedded FBG sensor was observed using an optical microscope. Figure 11 presents the cross-sectional micrograph of Sensor A. A small interfacial crack was observed between the facesheet and the arrester. The crack passed directly above the FBG sensor, indicating that the crack released strain in the FBG sensor (Fig. 12). Accordingly, we simulated the sensor response considering the interface crack. First, a crack between the arrester and the facesheet was introduced in the ENF specimen model (Fig. 4(b) with $L = 0$ mm), and the strain state in the FBG sensor was calculated. The reflection spectrum was then simulated by following the procedure described in Section 3.2. Figure 13 depicts the obtained spectrum. The thermal residual strain and the mechanical strain were almost completely released, and the difference between the maximum and minimum principal strains at the core (i.e., $\varepsilon_1 - \varepsilon_2$ in equation (1)) became almost zero. Consequently, the spectrum recovered its original shape. This result indicates that a crack penetrating the arrester can be detected from recovery of the spectrum

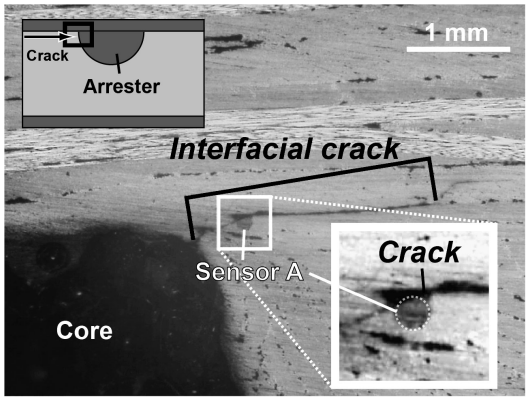

Figure 11. Cross-sectional micrograph of interface crack.

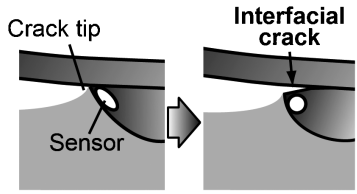

Figure 12. Schematics of sensor deformation before and after interfacial crack formation.

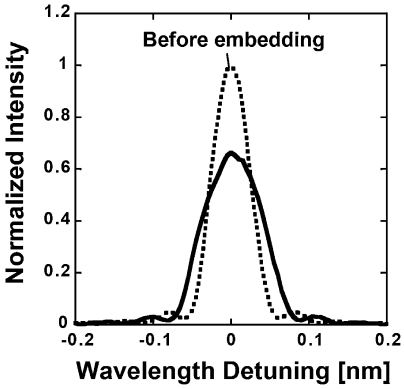

Figure 13. Simulated reflection spectrum of Sensor A of the ENF specimen after considering penetrating interface crack in FEA. The spectrum shape agreed well with the measured spectrum in Fig. 9(c).

shape. The penetrating crack critically degrades structural integrity and leads to catastrophic failures. Thus, spectral shape recovery can be considered as a distinct warning that loss of structural integrity is an imminent threat.

To summarize the verification tests, we could detect a crack approaching the crack arrester from the splitting of the spectrum, and a crack penetrating the arrester from the recovery of the spectrum shape. The proposed technique enables effective application of the crack arrester and thereby results in significant improvement of

the damage tolerance of foam-cored sandwich structures. In future work, the technique will be extended to more practically relevant 3-D plate structures by utilizing fiber-optic-based distributed strain measurement systems [22]. The validity of the technique under more complicated 3-D strain state should be verified through comprehensive tests using sandwich panel specimens with an arrester grid (Fig. 1). As foreseen by the authors, this technique is also valid with plate structures, since it is based on the particular strain state induced when the crack arrester suppresses interfacial crack, and thus is independent of global deformation of the structures.

5. Conclusions

A technique for detecting arrested cracks in foam-core sandwich structures was developed. First, FEA was conducted to predict the reflection spectra from the FBG sensors embedded at both edges of the crack arrester, validating the feasibility of the proposed technique. Verification tests clearly demonstrated that a crack approaching the arrester and a crack penetrating the arrester could be separately detected using the spectral responses. The proposed technique enables effective application of the crack arrester and thereby enables significant improvement of the damage tolerance of foam-core sandwich structures.

References

1. D. Zenkert (Ed.), *The Handbook of Sandwich Construction*. EMAS Publishing, Warrington, UK (1997).
2. J. R. Vinson, *The Behavior of Sandwich Structures of Isotropic and Composite Materials*. Technomic Publishing Company, Lancaster, USA (1999).
3. Y. Hirose, K. Kosugi, M. Nishitani, H. Sashikuma, M. Imuta, H. Fukagawa and H. Kikukawa, The CFRP sandwich panel for aircraft nose structure, in: *Proc. 23rd Intl Congr. Aeronaut. Sci.*, pp. 343.1–343.10 (2002).
4. A. S. Herrmann, P. C. Zahlen and I. Zuardy, Sandwich structures technology in commercial aviation: present applications and future trends, *Proc. 7th Intl Conf. Sandwich Struct. (ICSS-7)*, pp. 13–26 (2005).
5. P. C. Zahlen, M. Rinker and C. Heim, Advanced manufacturing of large, complex foam core sandwich panels, in: *Proc. 8th Intl Conf. Sandwich Struct. (ICSS8)*, pp. 606–623 (2008).
6. M. Burman and D. Zenkert, Fatigue of foam core sandwich beams-1: undamaged specimens, *Intl J. Fatigue* **19**, 551–561 (1997).
7. A. Shipsha, S. Hallstrom and D. Zenkert, Failure mechanisms and modelling of impact damage in sandwich beams — A 2D approach: Part I — Experimental investigation, *J. Sandwich Struct. Mater.* **5**, 7–31 (2003).
8. F. Avilés and L. Carlsson, Experimental study of debonded sandwich panels under compressive loading, *J. Sandwich Struct. Mater.* **8**, 7–31 (2006).
9. J. L. Grenestedt, Development of a new peel-stopper for sandwich structures, *Compos. Sci. Technol.* **61**, 1555–1559 (2001).
10. J. Jakobsen, E. Bozhevolnaya and O. T. Thomsen, New peel stopper concept for sandwich structures, *Compos. Sci. Technol.* **67**, 3378–3385 (2007).

11. J. Jakobsen, O. T. Thomsen, E. Bozhevolnaya and J. H. Andreasen, Crack deflection analyses of different peel stopper designs for sandwich structures, *Compos. Sci. Technol.* **69**, 870–875 (2009).
12. E. Bozhevolnaya, J. Jakobsen and O. T. Thomsen, Fatigue performance of sandwich panels with peel stoppers, *Strain — Intl J. Exper. Mech.* **45**, 349–357 (2009).
13. J. Jakobsen, J. H. Andreasen and O. T. Thomsen, Crack deflection by core junctions in sandwich structures, *Engng Fract. Mech.* **76**, 2135–2147 (2009).
14. Y. Hirose, M. Hojo, A. Fujiyoshi and G. Matsubara, Suppression of interfacial crack for foam core sandwich panel with crack arrester, *Adv. Compos. Mater.* **16**, 11–30 (2007).
15. H. Matsuda, G. Matsubara, Y. Hirose and M. Hojo, Effect of crack arrester for foam core sandwich panel under mode I, mode II and mixed-mode condition, in: *Proc. 16th Intl Conf. Compos. Mater*, FrKA1-02 (2007).
16. Y. Hirose, H. Matsuda, G. Matsubara, F. Inamura and M. Hojo, Evaluation of new crack suppression method for foam core sandwich panel *via* fracture toughness tests and analyses under mode-I type loading, *J. Sandwich Struct. Mater.* **11**, 451–470 (2009).
17. A. Othonos and K. Kalli, *Fiber Bragg Gratings: Fundamentals and Applications in Telecommunications and Sensing*. Artech House Publishers, Norwood, USA (1999).
18. R. Gafsi and M. A. El-Sherif, Analysis of induced-birefringence effects on fiber Bragg gratings, *Optic. Fiber Technol.* **6**, 299–323 (2000).
19. A. P. Zhang, B. O. Guan, X. M. Tao and H. Y. Tam, Experimental and theoretical analysis of fiber Bragg gratings under lateral compression, *Optics Comm.* **206**, 81–87 (2002).
20. Y. Okabe, Y. Shigeki, R. Tsuji, T. Mizutani and N. Takeda, Effect of thermal residual stress on the reflection spectrum from fiber Bragg grating sensors embedded in CFRP laminates, *Compos. Part A: Appl. Sci. Manuf.* **33**, 991–999 (2002).
21. K. Peters, P. Pattis, J. Botsis and P. Giaccari, Experimental verification of response of embedded optical fiber Bragg grating sensors in non-homogeneous strain fields, *Optics Lasers Engng* **33**, 107–119 (2000).
22. K. Kishida and C. H. Li, Pulse pre-pump-BOTDA technology for new generation of distributed strain measuring system, in: *Structural Health Monitoring and Intelligent Infrastructure*, J. Ou, H. Li and Z. Daun (Eds), pp. 471–477. Taylor and Francis, Oxfordshire, UK (2006).